Vector signatures of adiabatic and diabatic dynamics in the photodissociation of ICN

Vector signatures of adiabatic and diabatic dynamics in the photodissociation of ICN

Matthew L. Costen, Simon W. North,[a] and Gregory E. Hall
Chemistry Department, Brookhaven National Laboratory, Upton, New York 11973-5000

(Received 28 June 1999; accepted 27 July 1999)

Nascent Doppler profiles of CN ($X\,^2\Sigma^+$) fragments from the $\tilde{A}$ band photodissociation of room temperature ICN have been measured using high-resolution transient frequency modulated absorption spectroscopy. Results for dissociation at 222 nm, 248 nm, 266 nm, and 308 nm are presented. From the Doppler profiles of multiple CN states, we determine branching ratios of the coincident atomic iodine states, and bipolar moments characterizing the CN velocity and angular momentum anisotropy. The measurements provide sensitive tests of the strengths of optical coupling to the excited states contributing to the $\tilde{A}$ band continuum, and the adiabatic and diabatic dynamics leading to the observed product states. Precise velocity measurements resolve differences in the average energy of the ICN molecules leading to selected fragment channels. We find a bond energy for ICN of $26\,980 \pm 100\,\mathrm{cm}^{-1}$, somewhat higher than previous literature values. © *1999 American Institute of Physics.* [S0021-9606(99)00939-3]

I. INTRODUCTION

In the advancing field of molecular photodissociation, a few molecules attract disproportionate attention from theorists and experimentalists alike. These are generally molecules with experimentally convenient dissociation frequencies and easily detected fragments, small enough to be theoretically tractable, and representing some larger class of photodissociations for which they may be considered prototypes. The photodissociation of cyanogen iodide (ICN) in the near-ultraviolet $\tilde{A}$ band is one such system.

Now, after extensive experimental[1–27] and theoretical investigations,[28–35] we know that ICN displays remarkable complexity in its photodissociation for a linear triatomic molecule. The $\tilde{A}$ band continuum, which extends from about 210 to 320 nm, includes unresolved contributions from several optically bright states. Photofragments include ground state ($^2P_{3/2}$) and spin–orbit excited ($^2P_{1/2}$) iodine atoms (hereafter I and I^*), along with a highly nonstatistical distribution of CN rotational states with very little vibrational energy. The CN product state distributions change substantially with photolysis wavelength,[3,4,8,10,12–14,20] but not so dramatically with temperature.[10,13] The I^*/I ratio goes through a maximum value near the center of the $\tilde{A}$ band, at around 260 nm.[5,6,18] Vector properties of the dissociation point to mixed parallel/perpendicular transitions. The velocity anisotropy, probed by photofragment translational spectroscopy[2] and by Doppler spectroscopy[14,20,23] shows a predominantly parallel nature to the absorption, with the I^* channel generally closer to the limit of pure parallel dissociation. Rotational alignment measurements[15,16] of the CN photofragments also point to mixed parallel/perpendicular absorption. Low rotational states of CN display negative alignments (rotation axis preferentially perpendicular to the photolysis polarization), and higher rotational states have alignments approaching zero. A large net orientation of the CN angular momentum has been observed,[19,21] alternately parallel and antiparallel to the angular momentum of circularly polarized photolysis light, as the fragment total angular momentum increases. This effect has been attributed to quantum interference between the different potential energy surfaces leading to the same products. The relative populations of F_1 and F_2 spin–rotation components of the CN rotational states oscillate as the CN rotational quantum numbers increase.[11,17] This effect, too, is attributed to interferences in the multisurface dissociation. The role of hot bands in the red wing of the absorption spectrum has been noted,[9,10,12] as well as the role of parent bending in the curve crossing probabilities leading to I or I^*.[22] Femtosecond spectroscopy has been applied to ICN dissociation,[36] as a test case for femtosecond transition state spectroscopy.

Doppler spectroscopy has given some of the most detailed insights into the photodissociation. Modest velocity resolution is sufficient to distinguish between I and I^* partner atoms for each spectroscopically selected CN state. This has permitted an experimental partitioning of the total CN rotational distribution into I and I^* channels at 266 nm[14] and at 248 nm.[20] In general, the fractional yield of I^* decreases with increasing CN rotation, or in other words, the I channel has a hotter CN rotational distribution than the I^* channel. Velocity anisotropy is qualitatively evident from the Doppler profiles measured in different geometries, and with careful analysis, richer details of the angular momentum polarization can be extracted. The most ambitious analysis of Doppler profiles from ICN photodissociation has been by Black.[23] Two high rotational states of CN, above the I^* threshold, have been analyzed in terms of three optically bright components excited at 248 nm. The Doppler profile analysis shows components of symmetry matching the predicted ex-

[a]Current address: Department of Chemistry, Texas A&M University, College Station, TX 77842.

cited states: a parallel transition to a $^3\Pi_{0+}$ state, and both A' and A'' components of a $^1\Pi_1$ state. Black provides a scholarly synthesis of the most recent experimental and theoretical progress.

The history of ICN photodissociation theory is also a long one, developing in parallel with experimental work. A new era followed the first publication of realistic *ab initio* excited state potential energy surfaces by Morokuma and co-workers.[29,37] Much of the earlier theoretical work has been reviewed in comparison with experiment and in the context of the new surfaces.[28] Five bright states have been computed as comprising the $\tilde{A}$ continuum. A bent $^3\Pi_{0+}(A')$ state, correlating diabatically to I^* is populated from the linear $^1\Sigma^+$ ground state by a parallel transition. Bent A' and A'' components of a $^1\Pi_1$ and a $^3\Pi_1$ state all correlate diabatically to ground state iodine and are populated by weaker perpendicular transitions centered to the blue and the red, respectively, of the $^3\Pi_{0+}$ transition. The A' component of the $^1\Pi_1$ state and the $(A')^3\Pi_{0+}$ state are coupled in the vicinity of their conical intersection outside the Franck–Condon region. All excited states are computed to be bent near the Franck–Condon region, and the bending coordinate assumes a crucial role in both the development of CN angular momentum and the probability of curve-crossing.[22,29] Extensive work has followed,[30–35] using these new surfaces or variants to calculate absorption spectra, fragment state distributions and vector properties, comparing with the large body of experimental measurements. The dynamics on multiple surfaces, including a conical intersection, has advanced ICN into a new tested for coherent reaction dynamics.

We have recently developed a variant of frequency modulation (FM) spectroscopy ideally suited for Doppler spectroscopy,[38–40] and have performed a comprehensive set of measurements on ICN photodissociation throughout the $\tilde{A}$ band. Preliminary results for 308 nm photolysis have already been reported.[26] The use of the red $A-X$ system to probe CN offers several advantages over the more common violet $B-X$ system: Q-branch rotational lines present only in the $A-X$ spectrum add greatly to the sensitivity of the Doppler profile data to many of the vector correlations, and the spectral blending of lines originating from F_1 and F_2 spin–rotation components of the CN states is absent in the $A-X$ spectrum, allowing these components to be measured separately, even for low rotational states. The very narrow linewidth of the cw probe laser does not contribute to the instrumental broadening of the experimental spectra, which depends only on the known thermal distribution of the parent ICN.

The aim of this paper is to provide detailed experimental observations of ICN dissociation across the $\tilde{A}$ continuum using FM Doppler spectroscopy. New measurements are presented at 222 nm, 248 nm, 266 nm, and 308 nm. Comparisons with previously published, Doppler-resolved laser-induced fluorescence (LIF) data can be made at 248 and 266 nm. Questions concerning the completeness of the semiclassical bipolar moment analysis of Doppler spectra[41] in the presence of coherent excitation of parallel and perpendicular bands[42,43,44] can be addressed with the present large set of low-noise, high-resolution Doppler profiles. For a survey of

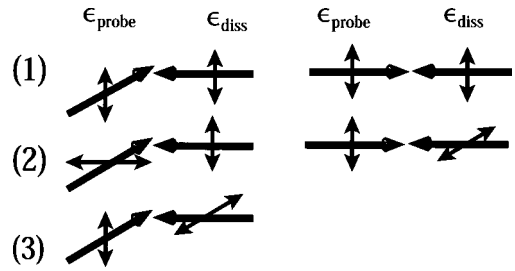

FIG. 1. Pump–probe geometries 1, 2, and 3 in coaxial and transverse propagation systems.

CN rotational states, sets of even, low order bipolar moments characterizing the correlated velocity-angular momentum distribution are determined in both I and I^* channels, at several wavelengths across the $\tilde{A}$ band. Many features of the state distributions, branching ratios and vector correlations are in good agreement with the current generation of multi-surface dynamics, although several questions remain open.

II. EXPERIMENT

The general features of the Brookhaven FM spectrometer have been described in some detail previously[26,38,40] and the modifications required to extract accurate Doppler lineshapes were the subject of a recent publication.[39] Briefly, a cw Ti:sapphire ring laser pumped by an Ar^+ laser and operating near 800 nm was frequency modulated at $\omega_m = 200$ MHz. The beam was attenuated to ~35 mW in a 3–4 mm diameter beam in the sample to avoid saturation of the CN molecular transitions, and steered through a 1.5 m single-pass glass cell. Dichroic mirrors combined the Ti:sapphire probe beam to co-propagate with photolysis light from a frequency quadrupled Nd:YAG laser at 266 nm (Spectra-Physics 170) or an excimer laser (Lambda Physik Compex 102) at 308 nm (XeCl), 248 nm (KrF), or 222 nm (KrCl). Excimer laser beams were polarized with a stack of 10 Brewster angle fused silica plates to give a measured 90% linear polarization; the quadrupled YAG laser beam was already highly polarized. In the collinear sample cell, measurements were made with linearly polarized pump and probe beams either parallel or perpendicular, geometries we will subsequently refer to as 1 and 2 (see Fig. 1). A second sample cell was used for a third, transverse geometry, only accessible in this cell. Here the probe beam made multiple (18–20) reflections between a pair of 1×3 inch flat, parallel mirrors, crossing the photolysis beam in the plane of the photolysis polarization and propagation. All three geometrical relationships between the probe laser propagation and polarization directions relative to the photolysis polarization direction may be realized in the transverse cell with appropriate control of the laser polarizations, and are shown in Fig. 1. The greater path length in the coaxial cell resulted in signals 5–6 times greater than in the transverse cell, and accordingly was preferred for geometries 1 and 2. For some scans using 266 nm photolysis the photolysis beam polarization was rotated through 90° using a photoelastic modulator (Hinds Instruments PEM 90). The timing of the photolysis laser was synchronized with the photoelastic modulator stress cycle to en-

able interleaved acquisition of scans in two experimental geometries, 1 and 3 in the transverse cell, or 1 and 2 in the longitudinal cell. Unfocused photolysis beams provided fluences of 2–10 mJ/cm^2 to the sample, with the exception of the 222 nm experiments from the weak KrCl excimer process, where the beam was loosely focused with a 2 m f.l. lens. The ground state ($X\,^2\Sigma$) CN radicals, produced from the laser photolysis, were probed in the $\Delta v=2$ bands of the $A\,^2\Pi \leftarrow X\,^2\Sigma$ system. A slow flow (2 sccm) of ICN (Aldrich or Eastman) was maintained with partial pressures of 5–30 mTorr at room temperature. Nascent signals were selected from the first 50 ns following photolysis. No appreciable relaxation of the lineshape occurs during this time. Thermalized lines were obtained for phase calibration by adding Ar to a total pressure of 1.0 torr, and selecting spectra 3–4 μs after photolysis. The photolysis entrance window accumulated a film of photolysis products, causing a slow decrease in transmission, and requiring cleaning after every few scans.

The phase-modulated beam transmitted through the sample cell was detected by a 1 GHz bandwidth photodiode. The photocurrent was separated with a bias-*T* into a DC component for intensity calibration and an AC component. The AC component was bandpass filtered, amplified with a 24 dB RF amplifier, and analyzed in an I&Q demodulator into in-phase and quadrature components. Following low pass filtration (<70 MHz), two channels (I&Q) of time-dependent FM signals were averaged in a digital oscilloscope and archived. A sequence of transient waveform pairs acquired at 100 MHz steps of the cw laser across single rotational lines comprises the archived data set, from which time-gated spectra are extracted for subsequent analysis. *Relaxed* spectra are fit to Gaussian absorption and dispersion line shapes to give an accurate phase angle calibration. This phase angle is used to combine the *nascent I* and *Q* spectra, removing any small dispersion component from a mixture of absorption and dispersion components. Previous studies from this laboratory[39,40] have used a modified integral transformation of the finite difference FM absorption line shapes to yield the underlying absorption line shape in the more familiar form. While the typical noise of the FM Doppler measurements can be very low, and the transformed line shapes are of high fidelity, for the most exacting error analysis, we can do better. The error propagation through the integral transformation makes a global least-squares fit inappropriate, as there are strong correlations between the errors of nearby spectral intensities in the transformed line shapes. We have modified our analysis routines to fit the phase-corrected FM line shapes directly, as will be described in the next section.

III. ANALYSIS

A. Fitting procedure

The shape of photofragment Doppler profiles is well known. The most widely used description is that of Dixon[41] in which the angular correlations between the transition dipole moment, $\boldsymbol{\mu}$, the fragment velocity, **v**, and the fragment angular momentum, **j**, are expanded in bipolar harmonics. For detection by single photon absorption with linearly polarized light, the Doppler-broadened absorption profile for an ensemble with a single velocity, v_0, can be written as

$$D(w)=\frac{1}{2v_0}\left[g_0+g_2P_2\left(\frac{w}{v_0}\right)+g_4P_4\left(\frac{w}{v_0}\right)\right], \tag{1}$$

where $w\leqslant v_0$ is the component of the laboratory velocity along the probe direction, P_2 and P_4 are Legendre polynomials, and the coefficients g_i depend on five low-order bipolar moments, $\beta_0^K(k_1k_2)$, of the correlated velocity and angular momentum distribution

$$g_0=1+b_1\beta_0^2(02), \tag{1.1}$$

$$g_2=b_2\beta_0^2(20)+b_3\beta_0^0(22)+b_4\beta_0^2(22), \tag{1.2}$$

$$g_4=b_5\beta_0^2(42). \tag{1.3}$$

The constants b_n are products of geometrical and angular momentum coupling factors, which depend in a simple way[41,45] on the angles between the photolysis polarization axis and the probe beam propagation and polarization directions, and on the probe transition (*P*,*Q*, or *R*). Corrections for incompletely polarized photolysis light and hyperfine nuclear depolarization are included in the b_n constants when appropriate.

When two electronic states of the iodine are populated in coincidence with a detected CN level, each channel has its own characteristic speed v_0. The Doppler profile is then a sum of two components, each with the form of Eq. (1), combined with weights f and $(1-f)$, the branching ratios for making I^* and I in coincidence with the detected CN quantum state:

$$D(w)=fD_{I^*}(w)+(1-f)D_I(w). \tag{2}$$

In a thermal ensemble of parent molecules, the center-of-mass velocity of each channel will additionally be broadened by the superposition of signals from parent molecules of different internal energies. In principle, the different vibrational states of ICN could produce the same fragment channel with different bipolar moments. The measured bipolar moments must be considered as incoherent weighted averages over initial states. We found adjustable energetic parameters to be required for each fragment channel in order to account for differences in effective parent energy, as described in Sec. IV A. The center-of-mass Doppler profiles are finally subject to a Gaussian convolution over the thermal velocity distribution of the parent molecules to produce the laboratory-frame Doppler profiles, which we designate as $D'(w)$. The additional instrumental broadening due to the linewidth of the cw ring laser is negligible.

When a Doppler-broadened absorption line is probed with frequency modulated light, the in-phase component of the beat signal detected at the modulation frequency depends on the differential absorption at the sideband frequencies. Rather than transforming the FM spectra to the ''integrated'' space of Doppler profiles, $D'(w)$, as we have previously done,[39,40] our optimum fits are performed on the FM spectra directly. The FM absorption signals are related to $D'(w)$ by finite difference according to

$$\mathrm{FM}(w) \propto D'(w-\delta) - D'(w+\delta) + \frac{J_1J_2 + J_2J_3}{J_0J_1 + J_1J_2} \times [D'(w-2\delta) - D'(w+2\delta)] + \frac{J_2J_3}{J_0J_1 + J_1J_2}[D'(w-3\delta) - D'(w+3\delta)] + \cdots . \quad (3)$$

Here δ is the modulation frequency, ω_m, expressed as an equivalent Doppler-shifted velocity,

$$\delta = \frac{\omega_m c}{\omega_0} \quad (4)$$

and the last two terms account for non-negligible higher-order sidebands,[46] expressed in terms of the Bessel functions J_n of argument M, the modulation index. Under our typical operating conditions, first-order sidebands were 25% of the residual intensity at the carrier frequency, corresponding to a modulation index of about 0.9. The first correction term in Eq. (3) then contributes about 20% of the total FM signal, and the second less than 1%. The higher-order terms not included in Eq. (3) have no detectable contribution to our measurements and have been neglected.

The common method used to determine the bipolar moments involves fitting measured lineshapes at different geometries and on different branches individually to a set of $P_0(w/v_0)$, $P_2(w/v_0)$ and (rarely) $P_4(w/v_0)$ basis functions, followed by extraction of the bipolar moments by solution of simultaneous Eqs. (1.1)–(1.3) for multiple data sets. A problem with this approach is that errors are introduced in both steps of the analysis. A simultaneous fitting of the Doppler profiles for all geometries and rotational branches of each CN fragment state permits a less biased parameter determination and a more rigorous error analysis.

We have used a simplex algorithm[47] for finding the least-squares best fit vector correlation parameters, branching ratio and energetic parameters. The total squared deviation between all observed FM Doppler profiles for a given CN quantum state and the simulated lines was minimized with respect to the desired fitting parameters. Several different parameter spaces were used to describe the vector correlations, and they are compared in Sec. IV C.

When recorded in separate scans, the relative intensities of different lines or the same line in different geometries are not experimentally determined to high precision. Therefore, in the global fits to multiple lines, each trial line is analytically scaled to the data before accumulating the sum of squared deviations between data and trial fit. When pairs of geometries are acquired in an interleaved fashion with a photoelastic modulator, the pairs of lines are forced to share a common scale factor, which includes the relative intensity information in the global fit.

B. Monte Carlo estimates of error bounds

The error limits on fitted parameters from Doppler profiles are usually difficult to estimate, as the measured bipolar moments are interdependent, and have definite physical ranges. A Monte Carlo analysis of the random measurement errors has been applied to characterize their propagation to the fitting parameters. An ensemble of synthetic, noisy FM spectra was generated by combining pseudorandom Gaussian noise with the best fits to an experimental data set. These synthetic FM spectra were then fit using the same routine as the experimental data. The resulting parameters were recorded for each of 1000 synthetic data sets to produce usable statistics. The quoted errors are 95% confidence limits from the distribution of individual parameters. Correlations between the variations in the fitted parameters are easily investigated as well. The energetic parameters were found to have very little correlation with the vector parameters. The errors were often distributed in a strongly non-normal fashion, particularly for parameters close to one of their physical limits. We have therefore cited unsymmetric confidence regions for many of our fitting parameters.

IV. RESULTS

A. Bond dissociation energy

The previous literature value for the ICN bond dissociation energy is $26\,500 \pm 500\ \mathrm{cm}^{-1}$, obtained from fits to LIF CN Doppler profiles.[14] The absence of laser bandwidth convolution effects and the high signal to noise ratio in the current FM measurements provide a high sensitivity to product speed distributions and allow us to improve on this result. Figure 2(a) shows FM Doppler spectra for the $R_1(0.5)$ line, probing the CN $(v=0, N=0)$ fragment state in two geometries (1 and 3), with 266 nm photolysis. These spectra were acquired in an interleaved fashion in the transverse cell using the photoelastic modulator to switch the polarization of the photolysis laser. These spectra are particularly simple to analyze, since this rotational state cannot display a rotational alignment and the I^* branching ratio is unity for this rotational state. The spectra depend only on the velocity anisotropy, $\beta_0^2(20)$, and a convolution over the available energy distribution. The velocity anisotropy may be canceled by adding Doppler spectra acquired in geometry 1 and geometry 3 with 2:1 weight, producing a composite profile that depends only on the product laboratory frame speed distribution. The resulting profile was fit by adjusting the I–CN bond energy and a vibrational temperature, describing the populations of the ICN vibrational levels. This fit, shown in Fig. 2(b), yielded a I–CN bond energy of $26\,980 \pm 100\ \mathrm{cm}^{-1}$ and a vibrational temperature of 400 ± 100 K. This provides our best estimate of the I–CN bond energy, as this nonrotating CN state is unlikely to have arisen preferentially from vibrationally excited parent molecules, and this value is consistent with the rest of our measurements. This value is at the top end of the uncertainty range reported by Wittig and co-workers,[14] 1100 cm^{-1} above the 1971 JANAF value,[48] and 900 cm^{-1} below the value reported by Chen and co-workers[49] in experiments quantitatively inconsistent with other investigations of ICN dissociation.

The wings of the Doppler spectra for higher rotational states are poorly fit assuming the same bond dissociation energy and parent internal energy distribution: the predicted Doppler profiles are too narrow. Similarly, the speeds of the I and I^* channel components of some CN states are closer

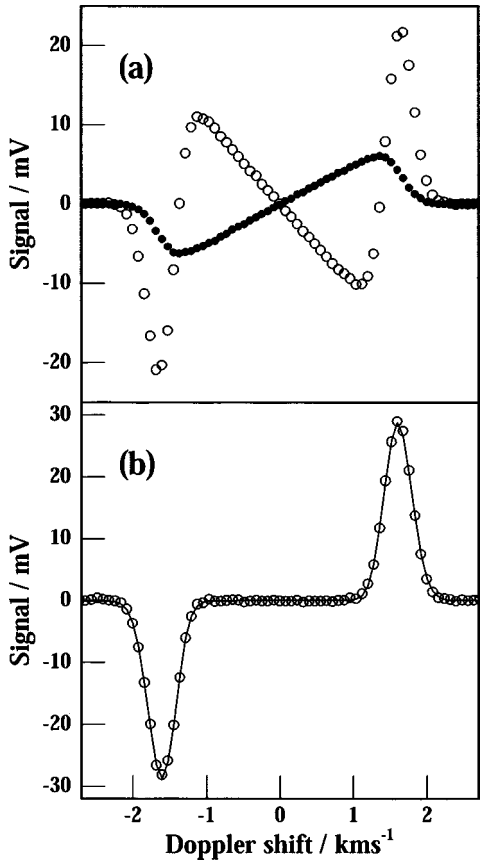

FIG. 2. $R(0)$ line from 266 nm photolysis (a) Geometries 1 (filled circles) and 3 (open circles) acquired simultaneously using the photoelastic modulator. (b) Composite speed dependent profile from these (open circles) with best fit to dissociation energy and Boltzmann parent internal energy distribution.

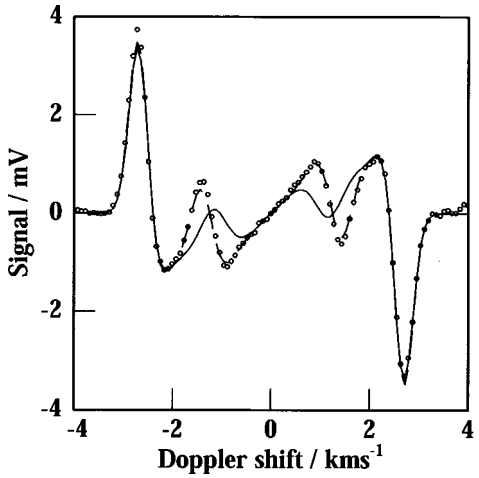

FIG. 3. Illustration of hot-band contributions to high rotational states in the I^* channel at 266 nm. Data points are for CN $N=30$, $v=0$ probed on the Q_1 branch in geometry 3. Dashed line is the best fit with separately adjusted available energies for I and I^* (fast and slow) channels. Solid line is the (poor) best fit obtainable without floating the I^* channel available energy.

together than one would expect from the known I^* energy. We ascribe this to variations in the average energy of that portion of the thermal ensemble leading to the selected fragment channel. The most stable and compact way we have found to represent this variation was to approximate the available energy distribution for each channel (I or I^*) of each CN rotational state as a Gaussian function with adjustable center and width. The energy available for CN internal energy and total translational energy in the center of mass is given by

$$E_{\text{avail}} = h\nu - D_0^0(I-\text{CN}) - E_{\text{SO}}(I/I^*) + E_{\text{int}}(\text{ICN}), \qquad (5)$$

where $E_{\text{SO}}(I/I^*)$ is either 0 or 7603 cm^{-1}. Changes in the available energy fitting parameter reflect differences in the average internal energy of the ensemble responsible for the detected fragment. The adjustable width parameter represents the spread of internal energy states of the parent leading to the detected fragment states, combined with the energy width of the photolysis laser.

Figure 3 shows an example for the $N=30$ state of CN formed at 266 nm. The illustrated Q_1 branch in the transverse geometry 3 most clearly shows the effect of different energetics for I and I^* channels. Assuming a bond dissociation energy of 26 980 cm^{-1}, the fast (I) channel is well described by an average parent energy of 320 cm^{-1} and a width of 570 cm^{-1}; the slow (I^*) channel is well fit with an average parent energy 800 cm^{-1} higher and a comparable width. If the I^* channel is forced to have an average available energy 7603 cm^{-1} less than the I channel, the fit is totally unacceptable, as shown in the solid line. Five spectra not shown (R-branch lines in three geometries and the other two Q-branch geometries) were included in both global fits for this rotational state of CN, differing only in the treatment of the I^* energetic parameters. The high rotational states of the I^* channel are clearly being formed selectively from vibrationally excited ICN molecules, as theoretically predicted.[29,35]

Table I summarizes the energetic parameters derived from the global fits to the measurements at several photolysis wavelengths, for selected CN rotational states, both I and I^* channels. The difference between the adjusted peak of the Gaussian available energy distribution and the calculated available energy from ICN molecules at 0 K (assuming a bond dissociation energy of $26\,980 \pm 100\,\text{cm}^{-1}$) is tabulated as a measure of the average internal energy of the ICN precursors for detected product states. The energy resolution of the Doppler velocity measurements decreases at high velocities, making the uncertainties larger at shorter photolysis wavelengths. We prefer to explain the small negative values for the apparent internal energy of ICN for fragments produced at 222 nm as measurement uncertainty, rather than as evidence for a higher ICN bond dissociation energy. The best values for the width parameter (Gaussian σ) typically fall in the range of 400–800 cm^{-1}, and correlation with other adjustable parameters was minimal. Three qualitative trends are evident in Table I. Higher rotational states of CN are preferentially produced from higher energy states of the parent ICN, the I^* channel for the same CN state is preferentially produced from hotter parent molecules, and these effects become stronger at longer photolysis wavelengths. These observations bear directly on the influence of parent vibrations on the absorption probability, nonadiabatic couplings, and on the dynamics of rotational excitation.

TABLE I. Average parent ICN internal energies for selected CN fragment channels[a].

Photolysis wavelength, nm	Rotational level, N	I channel average ICN internal energy, cm^{-1}	I^* channel average ICN internal energy, cm^{-1}
222	20	-500 ± 600	-100 ± 400
222	24	-200 ± 600	0 ± 400
222	30	-200 ± 600	-100 ± 400
222	40	-400 ± 600	100 ± 400
222	50	-200 ± 600	300 ± 400
222	60	300 ± 600	
222	65	500 ± 600	
248	4		300 ± 350
248	15	-100 ± 300	-100 ± 300
248	24	200 ± 200	550 ± 150
248	30	200 ± 200	400 ± 150
248	40	150 ± 150	1400 ± 300
248	46	200 ± 150	
248	50	300 ± 200	
266	0		250 ± 100
266	4		500 ± 200
266	15		500 ± 150
266	24	300 ± 200	800 ± 200
266	30	300 ± 150	1200 ± 200
266	40	500 ± 150	
266	46	700 ± 150	
266	50	500 ± 150	
266	55	850 ± 150	
308	20	800 ± 200	
308	30	950 ± 200	
308	40	1250 ± 200	

[a]Derived from the difference between $h\nu - D_0^0 - E_{SO}(I/I^*)$ and the fit parameter for the peak of the assumed Gaussian distribution of available energy. D_0^0 is taken to be $26\,980\pm100\ cm^{-1}$.

B. Rotational alignment

The Doppler-integrated rotational alignment, $A_0^{(2)}$, is twice the ensemble average of $P_2(\hat{\mathbf{j}}\cdot\hat{\mathbf{z}})$, the second Legendre polynomial of the cosine of the angle between the fragment angular momentum $\mathbf{j}$ and the space fixed $\hat{\mathbf{z}}$ direction defined by the photolysis polarization axis. Previous measurements have been reported based on LIF intensity measurements with switching of the linear polarization of either photolysis or probe laser.[15,16] The bipolar moment $\beta_0^2(02)$ conveys identical information, although it is defined in the frame of the parent molecular transition moment μ, which is itself aligned with a $\cos^2\theta$ distribution with respect to the laboratory $\mathbf{z}$ axis. When I and I^* channels are both present, a weighted average rotational alignment will be determined from the intensity ratio measurements without Doppler resolution. We have found that the precision of the FM Doppler measurements is adequate to extract reliable rotational alignment values, even for the separate I and I^* channels of each detected CN rotational state, without recourse to independent relative intensity information.

As an example, we have compared rotational alignments from the literature,[15,16] and from our global fits to independently normalized lineshapes in Table II. The $I+I^*$ channel-weighted values of the rotational alignment determined from the global line shape fits agree with the more direct intensity ratio determinations within the combined experimental uncertainties. Monte Carlo error analysis indicates that the sensitivity to the rotational alignment is good enough to make these values as reliable as those determined from intensity ratios. In a few test cases, we have performed global fits to FM Doppler signals using a value of the rotational alignment fixed by our measured intensity ratios or from the literature, and compared the results with the fits where the rotational alignment was floated freely. We find the optimum values of the other parameters to be relatively insensitive to reasonable choices of a fixed alignment. The one exception is the $\beta_0^2(42)$ moment, which is weakly correlated with $\beta_0^2(02)$. This is to be expected, since the measurements provide a secure determination of the ratio g_4/g_0. Equations (1.1) and (1.3) then imply a positive correlation between the errors in these bipolar moments.

TABLE II. Comparison of CN fragment quadrupole rotational alignments, $A_0^{(2)}$ determined by fitting Doppler profiles and from LIF intensity ratios.

λ(nm)	N	$A_0^{(2)}$ Doppler[a]	$A_0^{(2)}$ LIF[b]
266	4	$-0.34^{+0.04}_{-0.06}$	-0.33 ± 0.08
266	15	$-0.34^{+0.06}_{-0.05}$	$-0.26\pm0.04(N=13)$
266	24	$-0.26^{+0.02}_{-0.02}$	$-0.20\pm0.04(N=23)$
266	30	$-0.23^{+0.02}_{-0.02}$	$-0.24\pm0.06(N=28)$
248	4	$-0.36^{+0.06}_{-0.04}$	-0.25 ± 0.07
248	15	$-0.24^{-0.02}_{-0.02}$	-0.26 ± 0.06
248	24	$-0.21^{+0.03}_{-0.03}$	-0.18 ± 0.06
248	30	$-0.14^{+0.13}_{-0.10}$	-0.21 ± 0.07
248	40	$-0.07^{+0.08}_{-0.08}$	-0.10 ± 0.07
248	46	$-0.04^{+0.03}_{-0.02}$	-0.11 ± 0.07
248	50	$-0.11^{+0.05}_{-0.04}$	-0.10 ± 0.07

[a]Present work, weighted average of separately determined I and I^* channels, F_1 component only.
[b]Alignment measurements at 266 nm (Ref. 15) and 248 nm (Ref. 16) are unresolved averages of I and I^* channels, F_1 and F_2 components.

C. Global fits to the FM Doppler spectra

For the global fits presented in this paper, we use the shapes of the FM Doppler lines for Q and R branch lines, usually measured in three different geometries. For rotational states of CN with both coincident states of the I atom, we broadly have five pieces of information from each measured FM Doppler line: the ratios g_2/g_0 and g_4/g_0 for the I and the I^* component of each line, and an apparent branching ratio $g_0(I^*)/[g_0(I)+g_0(I^*)]$. Two rotational branches in three geometries gives effectively 30 measurements, exclusive of the energetic parameters discussed above. We seek a branching ratio and energetic parameters for the I and I^* channels, and five bipolar moments to characterize the vector correlations of each channel, still a heavily overdetermined set of measurements, despite the high dimensionality of the parameter space. The energetic parameters adjust the basis functions of the fit, and the vector parameters give the expansion coefficients. Rotational states of CN with only one coincident state of the I atom provide two pieces of informa-

tion per line, or twelve measurements from which we wish to extract five bipolar moments. Systematic residuals could always be eliminated in this parameter space, although an alternate, lower dimensional, representation of the vector correlations was also implemented and found to be very satisfactory.

Incoherent linear combinations of the five orthogonal limiting cases of the relative directions of **v**, **j**, and $\boldsymbol{\mu}$ described by Dixon[41] as cases $A-E$ have been used implicitly or explicitly by most experimentalists attempting to interpret measured bipolar moments.[50] The normalization constraint of the five fractional amplitudes makes this a four-dimensional subspace of the five-dimensional observable vector correlations. A constraint defining the incoherent subspace is that the $\beta_0^2(42)$ moment is not a free parameter, but determined by lower order moments, according to

$$\beta_0^2(42)=\tfrac{7}{12}\beta_0^2(02)-\tfrac{5}{12}\beta_0^2(22). \tag{6}$$

This constraint is equivalent to neglecting the molecular-frame alignment parameter, $\mathrm{Re}[a_1^2(\parallel,\perp)]$ in the notation of Rakitzis and Zare,[44] or the $\mathrm{Re}[f_2(1,0)]$ dynamical function in the notation of Siebbeles *et al.*[42] Deviations from Eq. (6) are a direct measure of this coherent term.

The adequacy of this four-dimensional, incoherent model has been tested in two ways. The first is to compare the optimum fits with and without the constraint of Eq. (6) applied. Many CN fragment states have been compared, particularly high rotational states, above the I^* threshold, where the analysis is most tightly constrained by the data. All of the measured lines could be fit in the lower dimensional, incoherent parameter space without systematic residuals outside the very small noise levels. Relaxing the constraint of Eq. (6) adds one additional degree of freedom to the parameter space, yet we find that the independent adjustment of all five bipolar moments generally does not produce significantly better fits. Figures 4 and 5 show examples of Doppler spectra and global fits with the incoherent model for two different CN rotational states. The $v=0, N=50, F_1$ state of CN from the 248 nm photolysis of ICN is shown in Fig. 4 as an example of a state for which only the I channel is accessible. The $N=30$ state from 248 nm photolysis is shown in Fig. 5 as an example when both I and I^* channels are present. The second test is to evaluate the deviation from Eq. (6) when all bipolar moments have been independently adjusted. Table III shows the results for a variety of single-channel CN fragment states and photolysis wavelengths. The best-fit values of $\beta_0^2(42)$ are compared to the combination of $\beta_0^2(02)$ and $\beta_0^2(22)$ that would equal $\beta_0^2(42)$ in the absence of coherence. The differences are small and rarely outside the combined Monte Carlo estimates of the error bounds. While there are good theoretical and experimental reasons to expect ICN photodissociation to be riddled with interference effects,[17,19,34] we find no justification in our data for the inclusion of the additional coherent parameter in our fits.

The incoherent representation of the bipolar moments as mixtures of cases $A-E$ has an appealing connection with the contributing excited state pathways, as previously described by Black.[23] Case *B*, with $\mathbf{v}\parallel\boldsymbol{\mu}\perp\mathbf{j}$, can be associated with a parallel transition, producing a limiting $\mathbf{v}\perp\mathbf{j}$ vector correlation, the signature expected for excitation to the $^3\Pi_{0+}$ state, regardless of its subsequent curve-crossing fate. Case *C*, with $\mathbf{v}\perp\boldsymbol{\mu}\parallel\mathbf{j}$, is the pattern expected for the A'' component of a perpendicular transition, and Case *E*, with $\mathbf{v}\perp\boldsymbol{\mu}\perp\mathbf{j}$, can be associated with the A' component of a perpendicular transition. Cases *A* and *D*, respectively, correspond to parallel and perpendicular transitions leading to $\mathbf{v}\parallel\mathbf{j}$, through a depolarization mechanism beyond the axial recoil approximation, when the total angular momentum is not negligible. A simple linear transformation connects the vector of fractional amplitudes for case $A-E$ contributions to a vector of bipolar moments.[45,49] Adjusting positive, normalized amplitudes for cases $A-E$ spans the same experimental space of Doppler spectra as adjusting the five bipolar moments, of Eq. (1), with the constraint of Eq. (6).

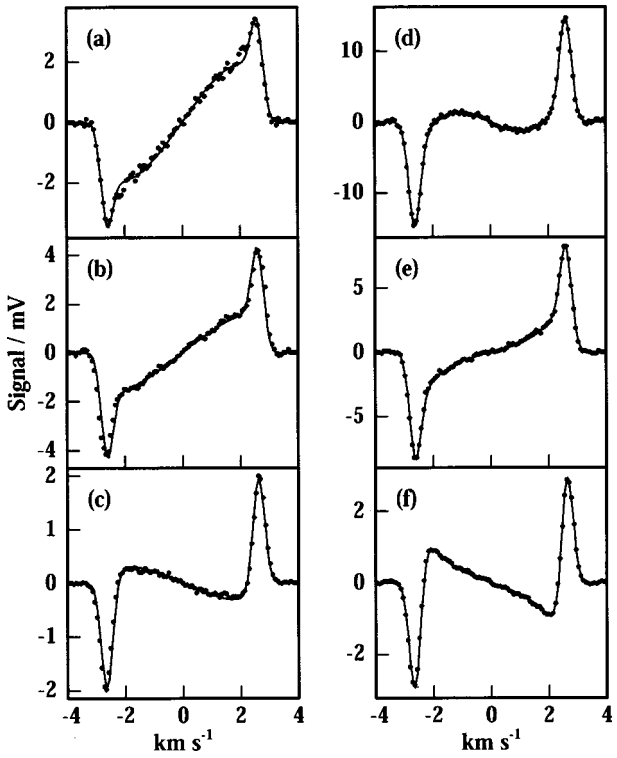

FIG. 4. FM Doppler spectra and fits for F_1 level of $N=50$ from 248 nm photolysis. (a)–(c) *R* branch in geometries 1–3, respectively, (d)–(f) *Q* branch in geometries 1–3, respectively. Circles are data points, solid lines are simultaneous fits to all six data sets using cases $A-E$ fit parameters.

One can attempt to reduce the parameter space for vector correlations even further. Additive mixtures of only cases *B*, *C*, and *E* were used by Black[23] to fit LIF Doppler data for $N=49$ and 58 CN produced at 248 nm, fragment states for which only ground state *I* is produced. The neglect of cases *A* and *D* is appropriate in the axial recoil limit for high-*j* fragments, and corresponds to fixing the $\mathbf{v}\cdot\mathbf{j}$ correlation at its limiting value of $\beta_0^0(22)=-0.5$. For comparison with Black's data and fits, we have analyzed the Doppler spectra for CN ($N=50, F_1$) shown in Fig. 4 in a variety of ways. When we fit only the *R* branch data in three geometries using a *BCE* model, the fits are excellent and the parameters (63% *B*, 27% *C*, 9% *E*) are within the error bounds cited by Black for his similar analysis of *R*-branch LIF data.[23] But when we examine the *Q* branch data, we find the simulated profiles

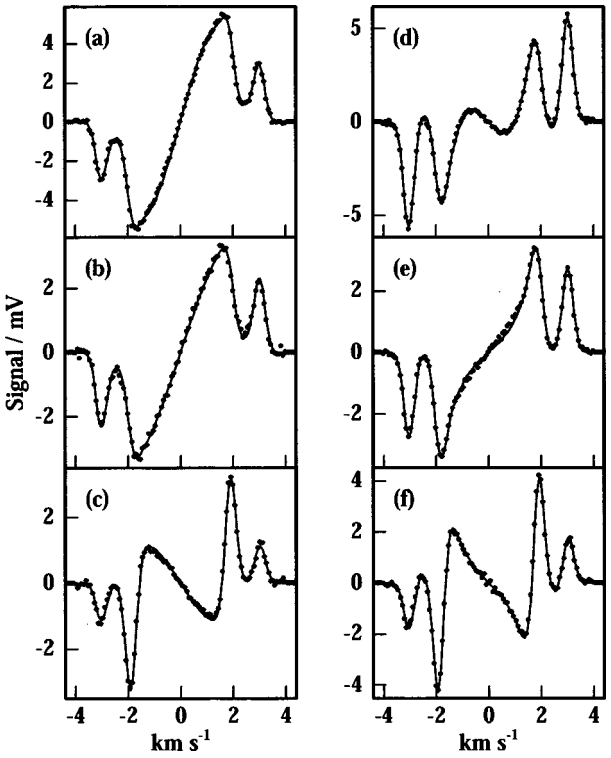

FIG. 5. FM Doppler spectra and fits for a state with both I and I^* channels, the F_1 level of $N=30$ from 248 nm photolysis. (a)–(c) R branch in geometries 1–3, respectively, (d)–(f) Q branch in geometries 1–3, respectively. Circles are data points, solid lines are simultaneous fits to all six data sets using cases $A-E$ fit parameters.

using these *BCE* parameters fail to reproduce the experiment, most noticeably for the Q branch in geometry 1, as shown in Fig. 6. Including the Q branch data and refitting with a *BCE* model makes little difference to the fit parameters or to the systematic residuals of the Q branch lines. Allowing the $\mathbf{v}\cdot\mathbf{j}$ correlation to deviate from its limiting perpendicular value, by including cases A and D in the fits, however, eliminates the systematic residuals in the fits for all three geometries on both branches, as shown in Fig. 4. Small, but non-negligible values of the A and D contributions to the fit, about 5% combined, correspond to a value of $\beta_0^0(22) = -0.42^{+0.02}_{-0.03}$. We conclude that the *BCE* parameter space is qualitatively adequate for describing the optical parentage of the detected photofragments, and should be increasingly accurate for rotationally cold samples, although quantitative fits to our Doppler spectra require allowance for deviations from limiting $\mathbf{v}\cdot\mathbf{j}$ correlations.

TABLE III. Test of coherent effects on CN Doppler spectra: comparison of $\beta_0^2(42)$ with the incoherent prediction.

λ(nm)	N	$\frac{7}{12}\beta_0^2(02)-\frac{5}{12}\beta_0^2(22)$	$\beta_0^2(42)$
222	60	-0.15 ± 0.05	-0.17 ± 0.05
222	65	-0.25 ± 0.05	-0.16 ± 0.05
248	46	-0.19 ± 0.04	-0.14 ± 0.04
248	50 F_1	-0.20 ± 0.02	-0.22 ± 0.02
248	50 F_2	-0.20 ± 0.02	-0.21 ± 0.02
266	40	-0.31 ± 0.02	-0.25 ± 0.02
266	46	-0.37 ± 0.02	-0.26 ± 0.02
266	50 F_1	-0.35 ± 0.03	-0.26 ± 0.03
266	50 F_2	-0.32 ± 0.03	-0.29 ± 0.03
266	55	-0.35 ± 0.03	-0.31 ± 0.03

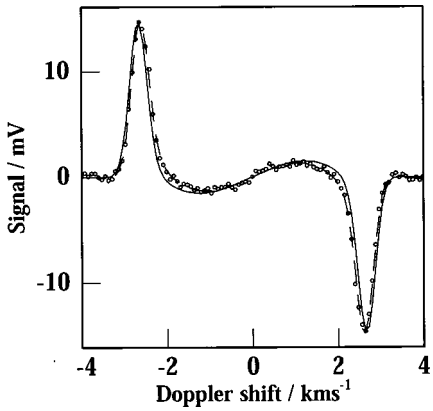

FIG. 6. Test of limiting $\mathbf{v}\cdot\mathbf{j}$ correlations for F_1 level of $N=50$ from 248 nm photolysis. Circles are data points for Q branch in geometry 1. Solid line (worse fit) is simulated using best fit parameters derived from R branch data only, restricted to cases B, C, and $E(\mathbf{v}\perp\mathbf{j})$. Dashed line is simulated using $A-E$ parameters derived from global fit to all Q and R lines.

In certain cases the full set of six lines are not available. Due to the lower absorption cross section at 222 nm and low photolysis fluence, we could not acquire useable data in the transverse cell. Remarkably, we found that two lines, each measured in the two coaxial geometries, can already provide a stable determination of the vector properties of the CN photofragments in the $A-E$ representation. Trial fitting of 248 nm data using all 6 lines or just Q and R lines in geometries 1 and 2 showed no significant variations in the fitted parameters, giving us confidence in the 222 nm results. Including data accessible only in the transverse cell tightened the confidence limits and improved the convergence, but did not produce systematic changes in the best vector parameters.

The Q_1 branch lines are blended with the R_{12} sub-branch at low rotational states. For the very lowest rotational states, when the spin-rotation splitting is less than the maximum Doppler shift, the Q_1 branch lines are difficult to analyze, and only the unblended R_1 branch lines have been included

TABLE IV. Comparison of bioplar moments for F_1 and F_2 spin rotation states for a variety of photolysis wavelengths.

λ_{diss}	N	$\beta_0^2(02)$	$\beta_0^2(20)$	$\beta_0^0(22)$	$\beta_0^2(22)$	$\beta_0^2(42)$
222	50 F_1 I	$-0.18^{+0.03}_{-0.01}$	$0.38^{+0.03}_{-0.02}$	$-0.46^{+0.01}_{-0.01}$	$0.24^{+0.01}_{-0.02}$	$-0.21^{+0.02}_{-0.01}$
222	50 F_2 I	$-0.24^{+0.01}_{-0.01}$	$0.46^{+0.01}_{-0.02}$	$-0.45^{+0.01}_{-0.01}$	$0.26^{+0.01}_{-0.01}$	$-0.25^{+0.01}_{-0.01}$
222	50 F_1 I^*	$-0.42^{+0.03}_{-0.03}$	$0.68^{+0.03}_{-0.04}$	$-0.44^{+0.02}_{-0.05}$	$0.23^{+0.03}_{-0.02}$	$-0.34^{+0.02}_{-0.03}$
222	50 F_2 I^*	$-0.32^{+0.03}_{-0.04}$	$0.67^{+0.03}_{-0.03}$	$-0.31^{+0.03}_{-0.03}$	$0.24^{+0.03}_{-0.02}$	$-0.29^{+0.02}_{-0.03}$
248	50 F_1 I	$-0.14^{+0.06}_{-0.05}$	$0.46^{+0.01}_{-0.02}$	$-0.42^{+0.02}_{-0.03}$	$0.31^{+0.02}_{-0.02}$	$-0.21^{+0.03}_{-0.02}$
248	50 F_2 I	$-0.16^{+0.05}_{-0.06}$	$0.53^{+0.02}_{-0.02}$	$-0.43^{+0.03}_{-0.02}$	$0.28^{+0.03}_{-0.02}$	$-0.21^{+0.03}_{-0.02}$
266	50 F_1 I	$-0.27^{+0.08}_{-0.08}$	$0.70^{+0.04}_{-0.03}$	$-0.42^{+0.04}_{-0.04}$	$0.36^{+0.03}_{-0.01}$	$-0.31^{+0.04}_{-0.04}$
266	50 F_2 I	$-0.26^{+0.07}_{-0.07}$	$0.70^{+0.05}_{-0.02}$	$-0.40^{+0.05}_{-0.02}$	$0.34^{+0.01}_{-0.02}$	$-0.29^{+0.04}_{-0.02}$

TABLE V. Best fit $A-E$ amplitudes for 222 nm photolysis.

N	A	B	C	D	E	Branching fraction
20 I	$0.00^{+0.01}$	$0.35^{+0.05}_{-0.08}$	$0.36^{+0.07}_{-0.05}$	$0.00^{+0.02}$	$0.29^{+0.03}_{-0.02}$	$0.65^{+0.03}_{-0.04}$
20 I^*	$0.00^{+0.02}$	$0.72^{+0.03}_{-0.03}$	$0.04^{+0.02}_{-0.02}$	$0.02^{+0.03}_{-0.02}$	$0.22^{+0.02}_{-0.02}$	$0.35^{+0.04}_{-0.03}$
24 I	$0.04^{+0.01}_{-0.02}$	$0.39^{+0.03}_{-0.02}$	$0.34^{+0.02}_{-0.01}$	$0.01^{+0.01}_{-0.01}$	$0.22^{+0.01}_{-0.01}$	$0.65^{+0.01}_{-0.02}$
24 I^*	$0.00^{+0.02}$	$0.75^{+0.01}_{-0.02}$	$0.06^{+0.01}_{-0.01}$	$0.00^{+0.01}$	$0.19^{+0.01}_{-0.01}$	$0.35^{+0.02}_{-0.01}$
30 I	$0.00^{+0.01}$	$0.45^{+0.03}_{-0.03}$	$0.27^{+0.02}_{-0.03}$	$0.00^{+0.01}$	$0.28^{+0.01}_{-0.02}$	$0.66^{+0.04}_{-0.04}$
30 I^*	$0.03^{+0.01}_{-0.01}$	$0.75^{+0.02}_{-0.01}$	$0.03^{+0.01}_{-0.01}$	$0.01^{+0.01}_{-0.01}$	$0.18^{+0.01}_{-0.01}$	$0.34^{+0.04}_{-0.04}$
40 I	$0.00^{+0.03}$	$0.51^{+0.03}_{-0.04}$	$0.26^{+0.03}_{-0.03}$	$0.03^{+0.01}_{-0.01}$	$0.20^{+0.01}_{-0.02}$	$0.78^{+0.04}_{-0.03}$
40 I^*	$0.14^{+0.02}_{-0.03}$	$0.62^{+0.07}_{-0.04}$	$0.07^{+0.02}_{-0.04}$	$0.03^{+0.02}_{-0.01}$	$0.14^{+0.01}_{-0.01}$	$0.22^{+0.03}_{-0.04}$
50 I	$0.00^{+0.01}$	$0.59^{+0.01}_{-0.02}$	$0.21^{+0.01}_{-0.01}$	$0.03^{+0.01}_{-0.01}$	$0.17^{+0.01}_{-0.01}$	$0.85^{+0.01}_{-0.01}$
50 I^*	$0.02^{+0.01}_{-0.02}$	$0.77^{+0.03}_{-0.02}$	$0.03^{+0.02}_{-0.02}$	$0.02^{+0.01}_{-0.02}$	$0.16^{+0.01}_{-0.02}$	$0.15^{+0.01}_{-0.01}$
60 I	$0.04^{+0.01}_{-0.01}$	$0.60^{+0.01}_{-0.01}$	$0.24^{+0.01}_{-0.01}$	$0.01^{+0.01}_{-0.01}$	$0.11^{+0.01}_{-0.01}$	1
65 I	$0.01^{+0.01}_{-0.01}$	$0.61^{+0.01}_{-0.01}$	$0.28^{+0.01}_{-0.01}$	$0.00^{+0.01}$	$0.10^{+0.01}_{-0.01}$	1

in the analysis. Tests using data sets where all six branches were available showed that restricting the R_1-branch only fits to cases *B, C,* and *E* (and hence $\mathbf{v}\perp\mathbf{J}$) reproduced the anisotropy and energy distributions within the statistical errors with only minor variations in the parameters other than the $\mathbf{v}\cdot\mathbf{j}$ correlation. Fits to low jR_1-branch data have thus been carried out in this further restricted parameter space. At higher rotational states, as the spin-rotation splitting exceeds the maximum Doppler shift, the low frequency half of the Q_1 line is unblended, and a symmetrized version of this half line was used in the fit. Finally, at the highest rotational levels, the satellite band intensities are very weak, and the splitting is large enough that the complete Q_1 branch lines can be used.

TABLE VI. Best fit $A-E$ amplitudes for 248 nm photolysis.

N	A	B	C	D	E	Branching fraction
4 I^*	0	$0.89^{+0.09}_{-0.01}$	$0.04^{+0.04}_{-0.03}$	0	$0.07^{+0.01}_{-0.06}$	1
15 I	0	$0.28^{+0.28}_{-0.10}$	$0.36^{+0.08}_{-0.12}$	0	$0.36^{+0.06}_{-0.09}$	$0.12^{+0.01}_{-0.06}$
15 I^*	0	$0.72^{+0.02}_{-0.02}$	$0.11^{+0.02}_{-0.02}$	0	$0.17^{+0.02}_{-0.02}$	$0.88^{+0.06}_{-0.01}$
24 I	$0.00^{+0.03}$	$0.47^{+0.02}_{-0.03}$	$0.30^{+0.01}_{-0.02}$	$0.03^{+0.01}_{-0.02}$	$0.20^{+0.01}_{-0.01}$	$0.28^{+0.01}_{-0.01}$
24 I^*	$0.07^{+0.01}_{-0.01}$	$0.77^{+0.01}_{-0.01}$	$0.04^{+0.01}_{-0.01}$	$0.02^{+0.01}_{-0.01}$	$0.10^{+0.01}_{-0.01}$	$0.72^{+0.01}_{-0.01}$
30 I	$0.00^{+0.09}$	$0.46^{+0.06}_{-0.11}$	$0.31^{+0.05}_{-0.04}$	$0.02^{+0.03}_{-0.02}$	$0.21^{+0.02}_{-0.03}$	$0.45^{+0.02}_{-0.01}$
30 I^*	$0.06^{+0.02}_{-0.02}$	$0.75^{+0.05}_{-0.01}$	$0.05^{+0.03}_{-0.03}$	$0.02^{+0.02}_{-0.02}$	$0.12^{+0.02}_{-0.02}$	$0.55^{+0.01}_{-0.02}$
40 I	$0.03^{+0.01}_{-0.01}$	$0.55^{+0.01}_{-0.01}$	$0.27^{+0.02}_{-0.02}$	$0.00^{+0.01}$	$0.15^{+0.02}_{-0.02}$	$0.93^{+0.02}_{-0.01}$
40 I^*	$0.07^{+0.09}_{-0.05}$	$0.57^{+0.06}_{-0.07}$	$0.14^{+0.14}_{-0.14}$	$0.05^{+0.10}_{-0.05}$	$0.17^{+0.08}_{-0.12}$	$0.07^{+0.01}_{-0.02}$
46 I	$0.03^{+0.01}_{-0.01}$	$0.60^{+0.01}_{-0.02}$	$0.26^{+0.02}_{-0.01}$	$0.00^{+0.01}$	$0.11^{+0.01}_{-0.01}$	1
50 I	$0.02^{+0.01}_{-0.01}$	$0.62^{+0.01}_{-0.01}$	$0.22^{+0.03}_{-0.03}$	$0.03^{+0.03}_{-0.02}$	$0.11^{+0.02}_{-0.02}$	1

TABLE VII. Best fit $A-E$ amplitudes for 266 nm photolysis.

N	A	B	C	D	E	Branching fraction
0 I^*	0	$0.95^{+0.02}_{-0.02}$	0	0	$0.05^{+0.02}_{-0.02}$	1
4 I^*	0	$0.85^{+0.05}_{-0.01}$	$0.05^{+0.03}_{-0.05}$	0	$0.10^{+0.04}_{-0.05}$	1
15 I^*	0	$0.80^{+0.02}_{-0.02}$	$0.05^{+0.04}_{-0.04}$	0	$0.15^{+0.05}_{-0.03}$	1
24 I	$0.05^{+0.01}_{-0.01}$	$0.66^{+0.01}_{-0.02}$	$0.18^{+0.01}_{-0.01}$	$0.01^{+0.01}_{-0.01}$	$0.10^{+0.01}_{-0.01}$	$0.35^{+0.01}_{-0.01}$
24 I^*	$0.07^{+0.01}_{-0.01}$	$0.78^{+0.01}_{-0.01}$	$0.05^{+0.01}_{-0.01}$	$0.03^{+0.01}_{-0.01}$	$0.07^{+0.01}_{-0.01}$	$0.65^{+0.01}_{-0.01}$
30 I	$0.00^{+0.01}$	$0.71^{+0.01}_{-0.01}$	$0.14^{+0.01}_{-0.01}$	$0.05^{+0.01}_{-0.01}$	$0.10^{+0.01}_{-0.01}$	$0.82^{+0.01}_{-0.01}$
30 I^*	$0.07^{+0.01}_{-0.01}$	$0.79^{+0.02}_{-0.02}$	$0.04^{+0.01}_{-0.01}$	$0.01^{+0.01}_{-0.01}$	$0.07^{+0.01}_{-0.01}$	$0.18^{+0.01}_{-0.01}$
40 I	$0.04^{+0.01}_{-0.01}$	$0.68^{+0.02}_{-0.02}$	$0.19^{+0.03}_{-0.03}$	$0.01^{+0.03}_{-0.01}$	$0.08^{+0.02}_{-0.02}$	1
46 I	$0.03^{+0.01}_{-0.01}$	$0.74^{+0.03}_{-0.03}$	$0.13^{+0.04}_{-0.01}$	$0.03^{+0.03}_{-0.03}$	$0.07^{+0.02}_{-0.02}$	1
50 I	$0.05^{+0.01}_{-0.02}$	$0.74^{+0.02}_{-0.03}$	$0.13^{+0.05}_{-0.04}$	$0.03^{+0.04}_{-0.03}$	$0.05^{+0.02}_{-0.02}$	1
55 I	$0.04^{+0.01}_{-0.01}$	$0.80^{+0.04}_{-0.01}$	$0.09^{+0.03}_{-0.03}$	$0.02^{+0.04}_{-0.02}$	$0.05^{+0.02}_{-0.03}$	1

In a few cases we have compared Doppler lineshapes for F_1 and F_2 components of same rotational state. Table IV compares bipolar moments derived from the two spin rotation components of the CN $N=50$ channel produced at 222 nm, 248 nm, and 266 nm. While the populations and perhaps the orientations have previously been found to vary with the spin–rotation levels,[14,21] the vector properties measured here are sometimes indistinguishable (as at 266 nm) and sometimes noticeably different (as at 222 nm). The theoretical basis[17] for understanding differences in the properties of the spin rotation components is less well developed than for other properties of the dissociation, and we have not investigated these effects in any great detail. For all the reported measurements other than those reported in Table IV, we have arbitrarily restricted our attention to the F_1 spin component of CN photofragments.

After this lengthy description of the fitting procedures, the best fit $A-E$ parameters are presented in Tables V–VIII for photolysis wavelengths 222, 248, 266, and 308 nm. The bipolar moments shown in Table IX–XII are an alternate representation of the same fits. The $\beta_0^2(42)$ values are well-determined by the data, but we emphasize that the constraint of Eq. (6) has been applied in the fitting as well as in the Monte Carlo error estimates. (This is in contrast to the values shown in Table III where five bipolar moments have been independently fit.) Figure 7 shows the rotational-state-resolved anisotropy parameters ($\beta=2\beta_0^2(20)$) for I and I^*

TABLE VIII. $A-E$ amplitudes from 308 nm photolysis.

N	A	B	C	D	E	Fraction I^*
20 I	$0.09^{+0.03}_{-0.02}$	$0.74^{+0.02}_{-0.02}$	$0.07^{+0.02}_{-0.02}$	$0.03^{+0.02}_{-0.02}$	$0.07^{+0.02}_{-0.03}$	0
30 I	$0.07^{+0.04}_{-0.03}$	$0.74^{+0.04}_{-0.03}$	$0.09^{+0.02}_{-0.03}$	$0.02^{+0.03}_{-0.02}$	$0.08^{+0.02}_{-0.03}$	0
40 I	$0.06^{+0.05}_{-0.04}$	$0.72^{+0.05}_{-0.05}$	$0.08^{+0.04}_{-0.03}$	$0.05^{+0.02}_{-0.03}$	$0.09^{+0.04}_{-0.03}$	0

TABLE IX. Bipolar moments from 222 nm photolysis.

N	$\beta_0^2(02)$	$\beta_0^2(20)$	$\beta_0^0(22)$	$\beta_0^2(22)$	$\beta_0^2(42)$
20 I	$0.03^{+0.10}_{-0.07}$	$0.03^{+0.08}_{-0.12}$	$-0.50^{+0.03}_{-0.00}$	$0.06^{+0.04}_{-0.04}$	$0.01^{+0.07}_{-0.15}$
20 I^*	$-0.44^{+0.03}_{-0.05}$	$0.58^{+0.04}_{-0.04}$	$-0.47^{+0.07}_{-0.03}$	$0.17^{+0.03}_{-0.04}$	$-0.33^{+0.03}_{-0.03}$
24 I	$0.07^{+0.04}_{-0.04}$	$0.14^{+0.02}_{-0.04}$	$-0.43^{+0.01}_{-0.02}$	$0.11^{+0.03}_{-0.01}$	$-0.00^{+0.03}_{-0.03}$
24 I^*	$-0.41^{+0.03}_{-0.01}$	$0.63^{+0.01}_{-0.01}$	$-0.50^{+0.04}_{-0.00}$	$0.22^{+0.01}_{-0.02}$	$-0.33^{+0.03}_{-0.01}$
30 I	$-0.10^{+0.03}_{-0.03}$	$0.19^{+0.05}_{-0.04}$	$-0.50^{+0.02}_{-0.00}$	$0.09^{+0.02}_{-0.02}$	$-0.09^{+0.03}_{-0.03}$
30 I^*	$-0.41^{+0.02}_{-0.03}$	$0.66^{+0.03}_{-0.01}$	$-0.43^{+0.01}_{-0.03}$	$0.18^{+0.01}_{-0.03}$	$-0.32^{+0.01}_{-0.03}$
40 I	$-0.10^{+0.05}_{-0.04}$	$0.27^{+0.06}_{-0.05}$	$-0.45^{+0.03}_{-0.01}$	$0.20^{+0.02}_{-0.02}$	$-0.14^{+0.03}_{-0.03}$
40 I^*	$-0.18^{+0.03}_{-0.08}$	$0.63^{+0.09}_{-0.03}$	$-0.24^{+0.03}_{-0.05}$	$0.08^{+0.06}_{-0.02}$	$-0.14^{+0.03}_{-0.07}$
50 I	$-0.18^{+0.03}_{-0.01}$	$0.38^{+0.03}_{-0.02}$	$-0.46^{+0.01}_{-0.01}$	$0.24^{+0.01}_{-0.02}$	$-0.21^{+0.02}_{-0.01}$
50 I^*	$-0.42^{+0.03}_{-0.03}$	$0.68^{+0.03}_{-0.04}$	$-0.44^{+0.02}_{-0.05}$	$0.23^{+0.03}_{-0.02}$	$-0.34^{+0.02}_{-0.03}$
60 I	$-0.08^{+0.01}_{-0.01}$	$0.47^{+0.01}_{-0.01}$	$-0.43^{+0.01}_{-0.01}$	$0.28^{+0.01}_{-0.01}$	$-0.17^{+0.01}_{-0.01}$
65 I	$-0.07^{+0.02}_{-0.02}$	$0.44^{+0.01}_{-0.02}$	$-0.49^{+0.01}_{-0.01}$	$0.34^{+0.01}_{-0.01}$	$-0.18^{+0.01}_{-0.01}$

channels at four photolysis wavelengths. Figures 8–10 each show for a different photolysis wavelength the I^* branching fraction for that wavelength as a function of N, the rotational distribution from the literature decomposed by the measured branching fraction into I and I^* channels, and stacked bar charts of the A through E amplitudes for each channel.

V. DISCUSSION

Much recent progress has been made by several groups in extending the formalisms of polarized photofragmentation.[42–44,51–54] In each case, the results can be recast as bipolar harmonics, which efficiently describe the number of observable parameters and their symmetries, given the number and polarization of photons used in the dissociation and detection steps. The functional forms of Eq. (1), appropriate for single photon, linearly polarized photolysis and probing, are here confirmed to a high degree of precision, without approximation or neglecting terms. In the presence of mixed symmetry excitations and mixed diabatic and adiabatic dynamics, the interpretation of the experimentally determined bipolar moments in terms of molecular properties becomes the issue of importance. No matter what language is used to describe the vector correlations, what one really hopes to understand is the underlying molecular dynamics. To us, in the case of ICN, this primarily means identifying the optically excited states, and the role of the bending coordinate in rotational excitation and in the branching between diabatic and adiabatic paths. The relative amplitudes of the B, C, and E parameters of Figs. 8–10 provide good qualitative answers to these questions. The neglect of small coherent terms and the small deviations from the axial recoil limit implied by nonzero case A and D amplitudes make this interpretation inexact, but many of the features of the multiple-surface photodissociation of ICN derived from previous experimental and theoretical work are clearly evident in the trends of the B, C, and E parameters. Finer points, including an analysis of our extended measurements using circularly polarized photolysis and probe lasers, will be reported separately.[55]

TABLE X. Bipolar moments from 248 nm photodissociation.

N	$\beta_0^2(02)$	$\beta_0^2(20)$	$\beta_0^0(22)$	$\beta_0^2(22)$	$\beta_0^2(42)$
4 I^*	$-0.45^{+0.05}_{-0.05}$	$0.84^{+0.13}_{-0.04}$	-0.5	$0.40^{+0.06}_{-0.05}$	$-0.43^{+0.05}_{-0.03}$
15 I	$0.04^{+0.13}_{-0.16}$	$-0.08^{+0.26}_{-0.19}$	-0.5	$-0.04^{+0.12}_{-0.11}$	$0.04^{+0.11}_{-0.14}$
15 I^*	$-0.34^{+0.01}_{-0.01}$	$0.58^{+0.01}_{-0.02}$	-0.5	$0.24^{+0.01}_{-0.01}$	$-0.30^{+0.01}_{-0.01}$
24 I	$-0.05^{+0.03}_{-0.03}$	$0.20^{+0.03}_{-0.03}$	$-0.46^{+0.04}_{-0.03}$	$0.19^{+0.02}_{-0.04}$	$-0.11^{+0.04}_{-0.02}$
24 I^*	$-0.34^{+0.01}_{-0.01}$	$0.75^{+0.01}_{-0.01}$	$-0.37^{+0.01}_{-0.01}$	$0.25^{+0.01}_{-0.01}$	$-0.30^{+0.01}_{-0.02}$
30 I	$-0.03^{+0.18}_{-0.11}$	$0.19^{+0.06}_{-0.07}$	$-0.47^{+0.15}_{-0.03}$	$0.19^{+0.06}_{-0.12}$	$-0.10^{+0.15}_{-0.08}$
30 I^*	$-0.34^{+0.05}_{-0.07}$	$0.71^{+0.05}_{-0.04}$	$-0.38^{+0.05}_{-0.09}$	$0.22^{+0.07}_{-0.03}$	$-0.29^{+0.03}_{-0.05}$
40 I	$-0.10^{+0.03}_{-0.03}$	$0.29^{+0.02}_{-0.02}$	$-0.44^{+0.03}_{-0.02}$	$0.22^{+0.03}_{-0.02}$	$-0.13^{+0.02}_{-0.02}$
46 I	$-0.05^{+0.03}_{-0.01}$	$0.43^{+0.02}_{-0.02}$	$-0.45^{+0.02}_{-0.01}$	$0.28^{+0.01}_{-0.01}$	$-0.15^{+0.02}_{-0.01}$
50 I	$-0.14^{+0.06}_{-0.05}$	$0.46^{+0.01}_{-0.02}$	$-0.42^{+0.02}_{-0.03}$	$0.28^{+0.02}_{-0.02}$	$-0.21^{+0.03}_{-0.02}$

TABLE XI. Bipolar moments from 266 nm photolysis.

N	$\beta_0^2(02)$	$\beta_0^2(20)$	$\beta_0^0(22)$	$\beta_0^2(22)$	$\beta_0^2(42)$
0 I^*	0	$0.92^{+0.03}_{-0.03}$	0	0	0
4 I^*	$-0.43^{+0.05}_{-0.07}$	$0.81^{+0.04}_{-0.04}$	-0.5	$0.38^{+0.05}_{-0.09}$	$-0.41^{+0.03}_{-0.05}$
15 I^*	$-0.43^{+0.06}_{-0.05}$	$0.85^{+0.05}_{-0.05}$	-0.5	$0.35^{+0.06}_{-0.06}$	$-0.44^{+0.02}_{-0.02}$
24 I	$-0.16^{+0.03}_{-0.02}$	$0.57^{+0.01}_{-0.01}$	$-0.41^{+0.02}_{-0.02}$	$0.28^{+0.02}_{-0.02}$	$-0.21^{+0.02}_{-0.02}$
24 I^*	$-0.32^{+0.01}_{-0.01}$	$0.79^{+0.01}_{-0.01}$	$-0.36^{+0.01}_{-0.01}$	$0.31^{+0.01}_{-0.01}$	$-0.32^{+0.01}_{-0.01}$
30 I	$-0.29^{+0.01}_{-0.01}$	$0.64^{+0.01}_{-0.02}$	$-0.50^{+0.03}_{-0.00}$	$0.36^{+0.01}_{-0.01}$	$-0.32^{+0.01}_{-0.01}$
30 I^*	$-0.30^{+0.01}_{-0.02}$	$0.86^{+0.02}_{-0.03}$	$-0.37^{+0.03}_{-0.02}$	$0.30^{+0.02}_{-0.01}$	$-0.30^{+0.01}_{-0.01}$
40 I	$-0.20^{+0.04}_{-0.07}$	$0.58^{+0.03}_{-0.03}$	$-0.45^{+0.04}_{-0.02}$	$0.33^{+0.05}_{-0.02}$	$-0.26^{+0.02}_{-0.04}$
46 I	$-0.23^{+0.07}_{-0.04}$	$0.67^{+0.03}_{-0.05}$	$-0.44^{+0.03}_{-0.05}$	$0.37^{+0.05}_{-0.01}$	$-0.29^{+0.03}_{-0.02}$
50 I	$-0.27^{+0.08}_{-0.08}$	$0.70^{+0.04}_{-0.03}$	$-0.42^{+0.04}_{-0.04}$	$0.36^{+0.03}_{-0.01}$	$-0.31^{+0.04}_{-0.04}$
55 I	$-0.28^{+0.04}_{-0.06}$	$0.77^{+0.05}_{-0.04}$	$-0.43^{+0.03}_{-0.04}$	$0.37^{+0.06}_{-0.01}$	$-0.32^{+0.03}_{-0.03}$

A. Comparison with previous work

The I^* branching ratios for 266 nm photolysis are identical to those extracted from previous LIF Doppler measurements,[14] although the slight variation in the velocity anisotropy with the CN rotational level shown in Fig. 7, was not previously detected. More significant differences are ob-

TABLE XII. Bipolar moments from 308 nm photolysis.

N	$\beta_0^2(02)$	$\beta_0^2(20)$	$\beta_0^0(22)$	$\beta_0^2(22)$	$\beta_0^2(42)$
20	$-0.18^{+0.05}_{-0.05}$	$0.79^{+0.02}_{-0.02}$	$-0.28^{+0.06}_{-0.05}$	$0.21^{+0.04}_{-0.04}$	$-0.19^{+0.04}_{-0.04}$
30	$-0.26^{+0.07}_{-0.06}$	$0.76^{+0.03}_{-0.02}$	$-0.36^{+0.07}_{-0.07}$	$0.28^{+0.04}_{-0.05}$	$-0.27^{+0.06}_{-0.05}$
40	$-0.25^{+0.11}_{-0.09}$	$0.72^{+0.02}_{-0.03}$	$-0.32^{+0.09}_{-0.07}$	$0.25^{+0.07}_{-0.07}$	$-0.25^{+0.08}_{-0.08}$

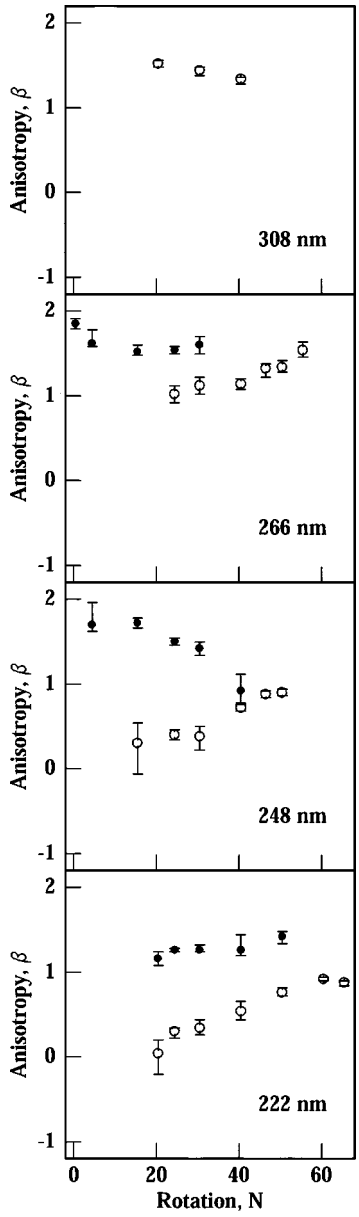

FIG. 7. Translational anisotropy, $\beta = 2\beta_0^2(20)$, as a function of product rotation, N, for the four photolysis wavelengths. Open circles are the I channel, filled circles the I^* channel.

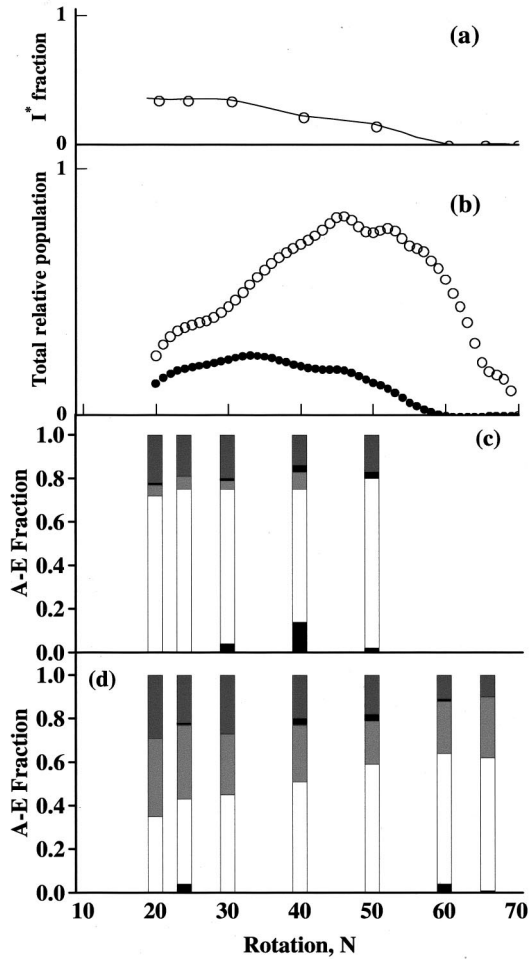

FIG. 8. Fitted parameters for 222 nm photolysis. (a) I^* branching fraction as a function of product rotation, open circles measured points, solid line is an interpolating spline to the points. (b) Rotational distribution from Ref. 12 decomposed into I (open circles) and I^* (filled circles) components. (c) Stacked bar chart of fitted $A-E$ fractions for the I^* channel, in bottom-to-top sequence A (black), B (white), C (gray), D (black), and E (dark gray). (d) Stacked bar chart of fitted $A-E$ fractions for the I channel, same sequence as in (c).

tained compared to the analysis of previous LIF Doppler measurements at 248 nm.[20,23] We find the velocity anisotropy of the I channel to show a much smaller perpendicular component than was previously extracted from lower resolution LIF data, although the qualitative trend toward lower β at low N is confirmed. The rotationally resolved I^* branching ratios at 248 nm are also quite different from previous reports, due to a correlation of errors in the branching ratio with the anisotropy in a single geometry.[20] Previous reports of 222 nm photodissociation of ICN have been limited to CN state distributions.[12] Theoretical spectral decompositions[30,33] based on the surfaces and transition moments of Morokuma and co-workers,[29] indicate that here on the blue side of the absorption spectrum, absorption to the $^1\Pi_1$ state should dominate over that of the $^3\Pi_{0+}$ state by factors of 3–6, resulting in an anisotropy between -0.5 and -0.25, averaged over all fragment states. Figure 7 shows our observations to give a state-averaged anisotropy of about $+0.8$, indicating that the parallel absorption is still dominant at this wavelength.

At 308 nm, the CN product is predominantly formed in a parallel dissociation. This is at odds with the theoretical predictions of excitation to the perpendicular $^3\Pi_1$ pair of surfaces, although consistent with earlier experimental work near 304 nm.[24] Although the I^* channel is closed at this energy, the $^3\Pi_{0+}$ surface is still accessible, particularly via hot bands, as it displays a well in the dissociation coordinate inside the crossing with the $^1\Pi_1$ surface. The reaction at this wavelength may thus proceed largely via excitation to the $^3\Pi_{0+}$ surface followed exclusively by adiabatic production of I on the $4A'$ surface. This would be enhanced by parent excitation in either the low frequency $I-C$ stretch (470 cm^{-1}) or the bend (321 cm^{-1}). The smaller perpendicular component to the dissociation then probably arises from the predicted $^3\Pi_1$ surfaces. The near identity of case C and E

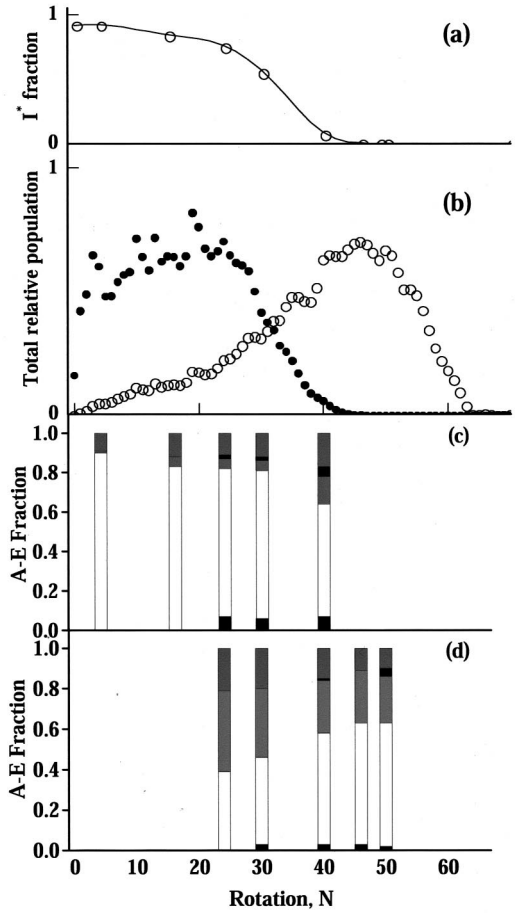

FIG. 9. Fitted parameters for 248 nm photolysis. Same as for Fig. 7 except (b) Rotational distribution from Ref. 16.

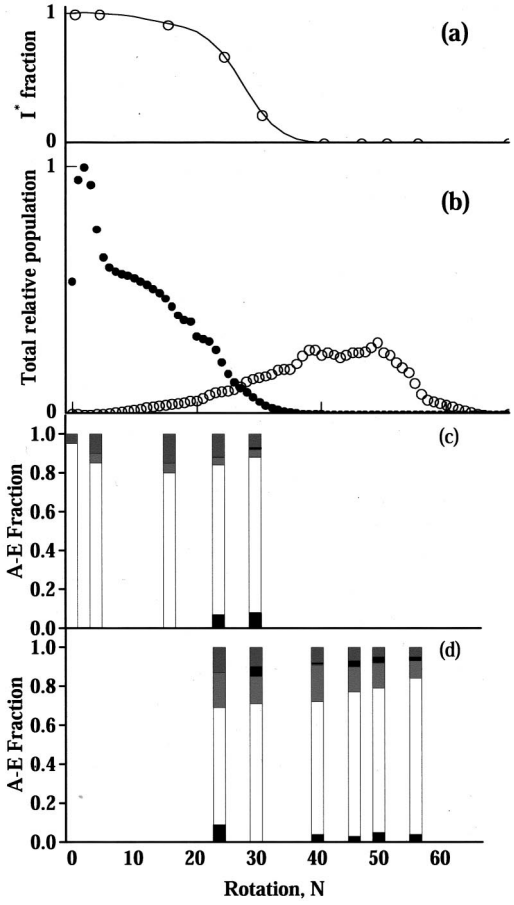

FIG. 10. Fitted parameters for 266 nm photolysis. Same as for Fig. 7 except (b) Rotational distribution from Ref. 14.

amplitudes, which can here be identified with the A'' and A' components of the $^3\Pi_1$ state, is consistent with this picture.

B. Adiabatic and diabatic dynamics

One of the most fascinating aspects of this multiple surface dissociation is the polarization labeling of different paths to the same products. In the axial recoil limit, a high j CN state formed in coincidence with I^* may have followed a diabatic path from the $4A'(^3\Pi_{0+})$ state, or an adiabatic path from the $5A'(^1\Pi_1)$ state. The diabatic path begins with a parallel transition and the adiabatic path begins with a perpendicular transition, implying that these two paths could be completely isolated by measuring fragments recoiling either parallel to or perpendicular to the polarization axis of the photolysis laser. A measurement of the anisotropy determines the relative contributions of the two paths. Coherence effects do not influence the velocity anisotropy, but only the rotational polarization,[42,56] just as orthogonal polarization states of light do not combine to produce an intensity interference pattern, but only a modulated polarization state.

Only two major pathways to CN in the I^* channel are evident in the $A-E$ fit parameters shown in Figs. 8–10: cases B and E. These can be associated with the diabatic and adiabatic A' paths. In contrast, CN in the I channel can be formed in three ways: an adiabatic path from the $4A'(^3\Pi_{0+})$ state, a diabatic path from the $5A'(^1\Pi_1)$ state and the uncoupled path from the A'' component of the $^1\Pi_1$ state. The addition of a significant case $C(A'')$ component in addition to B and E is clear in the fitting parameters for the I channel data. This interpretation was recognized by Black[23] as the explanation for the variation of the rotational alignment data with CN rotational states: the low rotational states come mostly from the I^* channel and show a strong negative alignment, due to a nearly pure A' origin. At higher rotational states, increasing contributions from the I channel permit an increasing A'' contribution, which can drive the alignment back toward zero. The present observations of different alignments for the I and I^* channels as a function of CN rotational state are a clear verification of this interpretation. From the Doppler spectra alone, a $^1\Pi_1$ or $^3\Pi_1$ state assignment cannot be made for case C and E contributions. We rely on the *ab initio* calculations[29] in our assumption that the $^3\Pi_1$ state is the dominant perpendicular excitation at 308 nm, and that the $^1\Pi_1$ state is the dominant perpendicular excitation at 266 nm and shorter wavelengths.

The variation of the nonadiabatic coupling of A' surfaces with bending angle is also clear from the rotationally dependent vector parameters, and fits quite well with the explanations of Amatatsu, Yabushita, and Morokuma.[29] Paths starting on the $4A'(^3\Pi_{0+})$ surface and passing near the conical intersection at small bending angles are more

likely to make a nonadiabatic transition up to the I^* asymptote, with low CN rotation. Paths starting on the $4A'(^3\Pi_{0+})$ surface and approaching the intersection at larger bending angles are more likely to follow the adiabatic path downward to the I asymptote, picking up more CN angular momentum after the avoided crossing. As a consequence, one expects and observes case B to dominate the low rotational levels in the I^* channel, and for case B to become increasingly dominant at higher rotational levels in the I channel.

From the rotationally averaged case E contribution to the I and I^* channels, we can estimate that the majority of the initial absorption to the $5A'(^1\Pi_1)$ surface follows an adiabatic path to I^* at 266 nm, switching over to a majority diabatic path to I at 222 nm, with intermediate behavior at 248 nm. This trend is what would be expected as the kinetic coupling between adiabatic surfaces increases at higher photolysis energy. The opposite trend is observed from the rotationally averaged case B contribution to I and I^* channels. Here the majority of the initial population excited to the $4A'(^3\Pi_{0+})$ surface follows the diabatic path to I^* at 266 nm, switching to a majority adiabatic path to I at 222 nm. Again, the 248 nm trend is intermediate. The different outcomes for different wavepackets approaching the same conical intersection is instructive. The smaller bending angles generated on the $4A'(^3\Pi_{0+})$ surface samples a stronger nonadiabatic coupling than the more bent wavepacket arriving from the $5A'(^1\Pi_1)$ surface at 266 nm, favoring the I^* path from both initial states. At 222 nm, the blue wing of the $4A'(^3\Pi_{0+})$ may be expected to favor the lower energy bent geometries, which develop angular momentum more rapidly than the more linear geometries sampled at the center of the absorption band. This could plausibly explain the trend to more adiabatic evolution of the $4A'(^3\Pi_{0+})$ excitation despite the higher photolysis energy.

C. ICN parent vibration

The room temperature samples of ICN used in this study have substantial population in the low frequency vibrational modes. Fewer than 60% of the molecules are in the vibrational ground state, and the vibrationally excited molecules can dissociate in ways that are quite different from ground state molecules. Rather than despairing at the ''unclean'' conditions of these experiments, we have taken advantage of subtle variations in fragment velocities to identify those fragment channels with larger than normal contributions from hot bands. The results are in qualitative accord with previous theoretical[29,32,33,35] and experimental[10,22] assessments of the effects of vibrational excitation on rotational excitation and curve crossing probabilities.

D. Nonlimiting v·j correlations

Our use of limiting cases B, C, and E to interpret the vector properties and surface crossing probabilities involves two approximations: negligible coherent contributions to the alignment and negligible deviations from limiting perpendicular $\mathbf{v}\cdot\mathbf{j}$ correlation, characterized by $\beta_0^0(22)=-0.5$. The neglect of coherent effects is justified experimentally, whereas relatively strong depolarization of the $\mathbf{v}\cdot\mathbf{j}$ correlation is sometimes observed in our data, and requires explanation. Previous tests for nonlimiting $\mathbf{v}\cdot\mathbf{j}$ correlations in the photodissociation of thermal cyanogen halides have led to conflicting results and interpretations.[20,23,57] No couplings, ''out-of-plane forces,'' or interference effects can produce a CN fragment from a $J=0$ parent ICN molecule with an angular momentum projection along its recoil axis in excess of 5/2 (3/2 when I^* is the co-fragment). For CN rotational states with $N=30$, these correspond to $\beta_0^0(22)\leqslant -0.490$ (-0.496 for I^*). Quantum descriptions of photofragment anisotropy and rotational polarization expressing the results as phased combinations of scattering states with total helicity restricted to 0 and ± 1 similarly require near-limiting $\mathbf{v}\cdot\mathbf{j}$ correlations.[42,51] The only plausible explanations for $\mathbf{v}\cdot\mathbf{j}$ depolarization are based on nonzero total angular momentum or errors in the measurements or analysis.

Even when the total angular momentum of the parent molecule is not zero, the axial recoil limit is often reached, and near-limiting negative $\beta_0^0(22)$ values are still expected. The axial recoil limit is reached when the Coriolis mixing of adjacent helicity states is negligible. Scattering states of total helicity up to total J may exist, but are not populated in the axial recoil limit following optical preparation of helicity states 0 and ± 1. Steep enough repulsive potentials and large enough excess energy will approach this limit for any fixed parent angular momentum state. A classical impulsive dissociation model for a rotating triatomic molecule described by Levene and Valentini[58] can be extended to treat vector correlations, and should provide a reasonable estimate of the onset of depolarization due to parent rotation.[59] One gauge of the deviation from the axial recoil limit is the reorientation angle between the molecular axis at the time of excitation and the asymptotic recoil direction. For typical thermally populated rotational states of ICN, the tangential velocity of the CN center of mass is 300–400 m/s. At a photolysis wavelength of 266 nm the high rotational states of CN fragment recoil from the center-of-mass at velocities of 1800–2500 m/s. These tangential and axial velocities correspond in the impulsive limit to recoil velocities deflected 7–12° from the initial bond direction. An exponential repulsion model[60] with a realistic potential parameter increases these angles by 10–20 %. A thermal average over parent rotation using the Levene and Valentini model produces a depolarized $\mathbf{v}\cdot\mathbf{j}$ correlation of $\beta_0^0(22)=-0.47$ for a $N=40$ fragment produced at 266 nm, compared to our experimental value of $-0.45^{+0.04}_{-0.02}$.

A second effect that can further depolarize the $\mathbf{v}\cdot\mathbf{j}$ correlation is vibrational angular momentum in the parent. A pre-existing angular momentum projection on the body-fixed axis of ICN will produce CN fragments with a component of $\mathbf{j}$ along $\mathbf{v}$ without the need for Coriolis mixing. Repeating the thermally averaged calculations for the $N=40$ fragment produced at 266 nm with a single quantum of vibrational angular momentum gives $\beta_0^0(22)=-0.46$, and two quanta of vibrational angular momenta give $\beta_0^0(22)=-0.45$. A similar calculation, scaled to the available energy of the 308 nm experiments, where the largest $\mathbf{v}\cdot\mathbf{j}$ depolarization has been observed, can account for $\beta_0^0(22)=-0.40$ with up to three quanta of vibrational angular momenta in the parent ICN.

This approaches the negative limit of our measured values, and is not totally unreasonable, given the selective excitation of high internal energy of those molecules excited by 308 nm. The high rotational levels in the I^* channel also tend to have larger than average $\mathbf{v}\cdot\mathbf{j}$ depolarization. These same channels are the ones which appear to originate preferentially from hot band excitation. In summary, simple thermal depolarization models come close to explaining the relatively large and precisely determined deviations from limiting $\mathbf{v}\cdot\mathbf{j}$ correlations. The remaining discrepancies may reflect the approximations of the simple depolarization model or unidentified systematic errors in our measurements or analysis.

E. Coherent effects in Doppler spectra

Recent investigations of coherent and incoherent contributions to the angular momentum distribution of products from linearly polarized photolysis have shown how the phase difference between multiple paths to the same final states may be extracted from a detailed analysis of the product velocity dependence of the angular momentum polarization.[42–44,61,62] The formalism of Rakitzis and Zare[44] may be transformed to an equivalent bipolar harmonic expansion,[63] and hence be related to the fit parameters used in this work. The translational anisotropy, β, and the $\mathbf{v}\cdot\mathbf{j}$ correlation, $\beta_0^0(22)$ are both incoherent properties, independent of interference terms. A large coherent alignment term would produce unmistakable effects on the other three bipolar moments, yet no such effect was detected. Because all of the data presented here are well described by a lower dimensional, incoherent model, we contend that coherent effects are not significant within our experimental precision and do not affect the broad conclusions of this work. After completing this analysis, we have realized that the small value of the coherent $\mathrm{Re}[a_1^2(\parallel,\perp)]$ term for the high-j CN fragments is a necessary consequence of the near-limiting negative values of a_0^2 for both parallel and perpendicular channels. Small physical limits are imposed on the interference term, regardless of the phase difference. The treatment of Siebbeles *et al.*[42] leads to the same conclusion. The dynamical function $\mathrm{Re}[f_2(1,0)]$ caries the same information as the $\mathrm{Re}[a_1^2(\parallel,\perp)]$ molecular frame alignment, and is the only coherent contribution to the dissociation that can be detected with linearly polarized light. Its normalized contribution to the polarization of high j fragments decreases as $1/j$, being proportional to $\sqrt{j}$ times the 3-j symbol $\begin{pmatrix} j & j & 2 \\ -1 & 0 & 1 \end{pmatrix}$.

We have recently collected a series of FM Doppler spectra with circularly polarized probe light and circularly polarized photolysis at 266 nm, similar to the LIF experiments of Zare and co-workers.[19,21] We find differences in the Doppler lineshapes as well as intensities as the photolysis polarization is switched from left to right handed. Bipolar moments in the μ-fixed frame used by Dixon to describe photofragment polarization are problematic for describing orientation effects,[64] but purely space-fixed bipolar moments allow a unified description of velocity dependent orientation and alignment. The intensity difference can be parametrized by $\beta_0^1(01)$, the total space-fixed orientation, and the orientation contribution to the P_2 part of the lineshape is carried in a $\beta_0^1(21)$ term. Each of these new bipolar moments is dominated by the $\mathrm{Re}[a_1^1(\parallel,\perp)]$ molecular frame orientation parameter, closely related to the dynamical function $\mathrm{Re}[f_1(1,0)]$. These results and a more extensive discussion of the influence of coherent processes on Doppler profiles within the bipolar moment formalism are deferred to a future publication.

VI. CONCLUDING REMARKS

The photodissociation of ICN is one of the most studied elementary unimolecular processes, yet it continues to provide new challenges. In this paper we have presented extensive new results from the application of high-resolution transient FM spectroscopy, providing a highly detailed look at this benchmark reaction. Within the incoherent model presented, the vector properties map both the relative transition probabilities to the dissociative surfaces and the probabilities of crossings between them. The results broadly agree with recent dynamical calculations based on the *ab initio* potential curves, although at both the red and blue wings of the absorption spectrum, more excitation to the parallel surface is seen than predicted. Both the surfaces and the transition moments could evidently be improved, although many qualitative trends and details are well reproduced.

Understanding the observable effects of coherence in multiple-surface reactions with mixed adiabatic and diabatic dynamics is a topic of much current interest.[65] Theoretical treatments isolating coherent and incoherent contributions to photofragment polarization are being tested and refined on diatomic and triatomic dissociations.[44,52,53,62,66] We hope the present and continuing measurements on diatomic fragments of well-studied, multiple-surface triatomic dissociations can help to clarify which interference effects persist in the semiclassical limit of high-j fragments and why.

ACKNOWLEDGMENTS

Helpful discussions with Dr. Peter Rakitzis and Dr. Yuxiang Mo concerning photofragment polarization are gladly acknowledged. This work was performed at Brookhaven National Laboratory under Contract No. DE-AC02-98CH1086 with the U.S. Department of Energy and supported by its Division of Chemical Sciences, Office of Basic Energy Sciences.

[1] See J. F. Black, J. R. Waldeck, and R. N. Zare, J. Chem. Phys. **92**, 3519 (1990) for a review of experimental work prior to 1990.
[2] J. H. Ling and K. R. Wilson, J. Chem. Phys. **63**, 101 (1975).
[3] M. J. Sabety-Dzvonik and R. J. Cody, J. Chem. Phys. **66**, 125 (1977).
[4] A. P. Baronavski and J. R. McDonald, Chem. Phys. Lett. **45**, 172 (1977).
[5] S. T. Amimoto, J. R. Wiesenfeld, and R. H. Young, Chem. Phys. Lett. **65**, 402 (1979).
[6] W. H. Pitts and A. P. Baronavski, Chem. Phys. Lett. **71**, 395 (1980).
[7] A. P. Baronavski, Chem. Phys. **66**, 217 (1982).
[8] W. Kreiger, J. Hager, and J. Pfab, Chem. Phys. Lett. **85**, 69 (1982).
[9] W. H. Fisher, T. Carrington, S. V. Filseth, C. M. Sadowski, and C. H. Dugan, Chem. Phys. **82**, 443 (1983).
[10] I. Nadler, H. Reisler, and C. Wittig, Chem. Phys. Lett. **103**, 451 (1984).
[11] F. Shokoohi, S. Hay, and C. Wittig, Chem. Phys. Lett. **110**, 1 (1984).
[12] W. H. Fisher, R. Eng, T. Carrington, C. H. Dugan, S. V. Filseth, and C. M. Sadowski, Chem. Phys. **89**, 457 (1984).
[13] W. J. Marinelli, N. Sivakumar, and P. L. Houston, J. Phys. Chem. **88**, 6685 (1984).

[14] I. Nadler, D. Mahgerefteh, H. Reisler, and C. Wittig, J. Chem. Phys. **82**, 3885 (1985).
[15] G. E. Hall, N. Sivakumar, and P. L. Houston, J. Chem. Phys. **84**, 2120 (1986).
[16] M. A. O'Halloran, H. Joswig, and R. N. Zare, J. Chem. Phys. **87**, 303 (1987).
[17] H. Joswig, M. A. O'Halloran, R. N. Zare, and M. S. Child, Faraday Discuss. Chem. Soc. **82**, 79 (1986).
[18] W. P. Hess and S. R. Leone, J. Chem. Phys. **86**, 3773 (1987).
[19] W. Hasselbrink, J. R. Waldeck, and R. N. Zare, Chem. Phys. **126**, 191 (1989).
[20] J. F. Black, J. R. Waldeck, and R. N. Zare, J. Chem. Phys. **92**, 3519 (1990).
[21] J. F. Black, E. Hasselbrink, J. R. Waldeck, and R. N. Zare, Mol. Phys. **71**, 11 (1990).
[22] P. W. Kash and L. J. Butler, J. Chem. Phys. **96**, 8923 (1992).
[23] J. F. Black, J. Chem. Phys. **98**, 6853 (1992); **100**, 5392 (1994)
[24] J. A. Griffiths and M. A. El-Sayed, J. Chem. Phys. **100**, 4910 (1994).
[25] K. Chen, C. Kuo, M. Tzeng, M. Shian, and S. E. Chung, Chem. Phys. Lett. **221**, 341 (1994).
[26] S. W. North, J. Mueller, and G. E. Hall, Chem. Phys. Lett. **276**, 103 (1997).
[27] K. J. Franks, H. Li, S. Kuy, and W. Kong, Chem. Phys. Lett. **302**, 151 (1999).
[28] See Ref. 29 for a review of theoretical work prior to 1994.
[29] Y. Amatatsu, S. Yabushita, and K. Morokuma, J. Chem. Phys. **100**, 4894 (1994).
[30] Y. Wang and C. X. W. Qian, J. Chem. Phys. **100**, 2707 (1994).
[31] Y. Wang and C. X. W. Qian, Chem. Phys. Lett. **219**, 389 (1994).
[32] J. M. Bowman, R. C. Mayrhofer, and Y. Amatatsu, J. Chem. Phys. **101**, 9469 (1994).
[33] J. Qian, D. J. Tannor, Y. Amatatsu, and K. Morokuma, J. Chem. Phys. **101**, 9597 (1994).
[34] H. Wei and T. Carrington, Jr., J. Chem. Phys. **105**, 141 (1996).
[35] F. N. Dzegilenko, J. M. Bowman, and Y. Amatatsu, Chem. Phys. Lett. **264**, 24 (1997).
[36] M. Dantus, R. M. Bowman, J. S. Baskin, and A. H. Zewail, Chem. Phys. Lett. **159**, 406 (1989), and references therein.
[37] S. Yabushita and K. Morokuma, Chem. Phys. Lett. **175**, 518 (1990).
[38] J. C. Bloch, R. W. Field, G. E. Hall, and T. J. Sears, J. Chem. Phys. **101**, 1717 (1994).
[39] S. W. North, X. S. Zheng, R. Fei, and G. E. Hall, J. Chem. Phys. **104**, 2129 (1996).
[40] S. W. North and G. E. Hall, J. Chem. Phys. **106**, 60 (1997).
[41] R. N. Dixon, J. Chem. Phys. **85**, 1866 (1986).
[42] L. D. A. Siebbeles, M. Glass-Maujean, O. S. Vasyutinskii, J. A. Beswick, and O. Roncero, J. Chem. Phys. **100**, 3610 (1994).
[43] B. V. Picheyev, A. G. Smolin, and O. S. Vasyutinskii, J. Phys. Chem. A **101**, 7614 (1997).
[44] T. P. Rakitzis and R. N. Zare, J. Chem. Phys. **110**, 3341 (1999).
[45] G. E. Hall and M. Wu, J. Phys. Chem. **97**, 10911 (1993).
[46] J. M. Supplee, E. A. Whittaker, and W. Lenth, Appl. Opt. **33**, 6294 (1994).
[47] W. H. Press, B. P. Flannery, S. A. Teukolsky, and W. T. Vettering, *Numerical Recipes* (Cambridge University Press, Cambridge, 1986), p. 312.
[48] *JANAF Thermochemical Tables*, 2nd Ed., edited by D. R. Stull and H. Prophet (U.S. GPO Washington, DC, 1971).
[49] K. Chen, C. Kuo, M. Tzeng, M. Shian, and S. E. Chung, Chem. Phys. Lett. **221**, 341 (1994).
[50] R. J. Gordon and G. E. Hall, Adv. Chem. Phys. **94**, 1 (1996).
[51] G. G. Balint-Kurti and M. Shapiro, Chem. Phys. **61**, 137 (1981).
[52] A. S. Bracker, E. R. Wouters, A. G. Suits, Y. T. Lee, and O. S. Vasyutinskii, Phys. Rev. Lett. **80**, 1626 (1998).
[53] A. S. Bracker, E. R. Wouters, A. G. Suits, and O. S. Vasyutinskii, J. Chem. Phys. **110**, 6749 (1999).
[54] Y. Mo and T. Suzuki, J. Chem. Phys. **108**, 6780 (1998).
[55] M. L. Costen and G. E. Hall (in preparation).
[56] D. V. Kupriyanov and O. S. Vasyutinskii, Chem. Phys. **171**, 25 (1993).
[57] E. A. J. Wannenmacher, H. Lin, W. H. Fink, A. J. Paul, and W. M. Jackson, J. Chem. Phys. **95**, 3431 (1991).
[58] H. B. Levene and J. J. Valentini, J. Chem. Phys. **87**, 2594 (1987).
[59] S. W. North and G. E. Hall (in preparation).
[60] R. Bersohn and A. H. Zewail, Ber. Bunsenges. Phys. Chem. **92**, 373 (1998).
[61] M. Ahmed, D. S. Peterka, A. S. Bracker, O. S. Vasyutinskii, and A. G. Suits, J. Chem. Phys. **110**, 4115 (1999).
[62] T. P. Rakitzis, S. A. Kandel, A. J. Alexander, Z. H. Kim, and R. N. Zare, J. Chem. Phys. **110**, 3351 (1999).
[63] T. P. Rakitzis, G. E. Hall, M. L. Costen, and R. N. Zare (in preparation).
[64] Y. Mo and T. Suzuki (private communication).
[65] R. J. Gordon and S. A. Rice, Annu. Rev. Phys. Chem. **48**, 601 (1997).
[66] Y. Mo, H. Katayanagi, and T. Suzuki, J. Chem. Phys. **110**, 2029 (1999).